Article

Axial Higgs mode detected by quantum pathway interference in RTe_3

https://doi.org/10.1038/s41586-022-04746-6

Received: 19 September 2021

Accepted: 8 April 2022

Published online: 8 June 2022

Check for updates

Yiping Wang[1], Ioannis Petrides[2], Grant McNamara[1], Md Mofazzel Hosen[1], Shiming Lei[3], Yueh-Chun Wu[4], James L. Hart[5], Hongyan Lv[6], Jun Yan[4], Di Xiao[7,8], Judy J. Cha[5], Prineha Narang[2], Leslie M. Schoop[3] & Kenneth S. Burch[1]✉

The observation of the Higgs boson solidified the standard model of particle physics. However, explanations of anomalies (for example, dark matter) rely on further symmetry breaking, calling for an undiscovered axial Higgs mode[1]. The Higgs mode was also seen in magnetic, superconducting and charge density wave (CDW) systems[2,3]. Uncovering the vector properties of a low-energy mode is challenging, and requires going beyond typical spectroscopic or scattering techniques. Here we discover an axial Higgs mode in the CDW system RTe_3 using the interference of quantum pathways. In RTe_3 (R = La, Gd), the electronic ordering couples bands of equal or different angular momenta[4–6]. As such, the Raman scattering tensor associated with the Higgs mode contains both symmetric and antisymmetric components, which are excited via two distinct but degenerate pathways. This leads to constructive or destructive interference of these pathways, depending on the choice of the incident and Raman-scattered light polarization. The qualitative behaviour of the Raman spectra is well captured by an appropriate tight-binding model, including an axial Higgs mode. Elucidation of the antisymmetric component is direct evidence that the Higgs mode contains an axial vector representation (that is, a pseudo-angular momentum) and hints that the CDW is unconventional. Thus, we provide a means for measuring quantum properties of collective modes without resorting to extreme experimental conditions.

Emergent order brings new modes whose properties are linked to a change in topology or symmetry. A well-studied example is the breaking of translation symmetry in charge density wave (CDW) systems, resulting in Nambu–Goldstone (phase) and Higgs (amplitude) modes. In a superconductor the inclusion of electromagnetism results in gapping of the phason or giving mass to the W and Z bosons of the electroweak theory. This Anderson–Higgs mechanism leaves the amplitude mode largely unchanged, and thus it is often referred to as the Higgs boson[2,3,7]. Despite its close resemblance to superconductivity and first prediction in 1958, all CDWs to date have revealed *s*-wave condensation with a scalar Higgs. Indeed, detecting unconventional order requires probing the vector nature of the order parameter or collective excitations: for example, attempts to extend the standard model by enlarging the symmetry breaking. This produces additional particles, including a spin-1 Higgs boson, and dark matter candidates[1]. Thus the detection of a Higgs mode with finite angular momenta (that is, an axial Higgs) heralds the discovery of a previously unseen symmetry breaking and phase of matter.

Pathway interference can meet this challenge by exploiting wave–particle duality to uncover quantum properties of excitations[8]. Quantum pathway interference has revealed the topological properties of band structures[9,10], unconventional superconducting order[11–13] and the non-trivial statistics of collective excitations[14–16]. Despite their elegance, these experiments have not been applied to the Higgs mode. In part, this results from the challenge of performing quantum interference in condensed matter settings, which typically require extreme experimental conditions: low temperatures, ultrafast lasers, high magnetic and/or electric fields. The need for such conditions could be overcome by CDW systems, with well-defined Higgs and phase modes readily observed using optical techniques at large energy scales[5,17–22]. Furthermore, the CDWs can be tuned by pressure, exfoliation or ultrafast lasers[23–25] and offer next-generation nano-oscillator, logic and memory devices[26].

Here we study quantum pathway interference of the axial Higgs mode to reveal the unconventional CDW phase in RTe_3. This is achieved at room temperature with Raman scattering, which measures the energy, symmetry and excitation pathways of modes[27–29]. We build on previous inelastic light-scattering experiments in non-interacting systems, which revealed chiral phonons, crystal field excitations, interband transitions and changes in quantum pathway or coherence on gating[30–33]. These previous single-particle experiments chose the intermediate states (that is, quantum pathways) by the combination of excitation wavelength, momentum conservation and light polarization via selection rules[34,35].

[1]Department of Physics, Boston College, Chestnut Hill, MA, USA. [2]John A. Paulson School of Engineering and Applied Sciences, Harvard University, Cambridge, MA, USA. [3]Department of Chemistry, Princeton University, Princeton, NJ, USA. [4]Department of Physics, University of Massachusetts Amherst, Amherst, MA, USA. [5]Department of Mechanical Engineering and Materials Science, Yale University, New Haven, CT, USA. [6]Key Laboratory of Materials Physics, Institute of Solid State Physics, HFIPS, Chinese Academy of Sciences, Hefei, China. [7]Department of Materials Science and Engineering, University of Washington, Seattle, WA, USA. [8]Department of Physics, University of Washington, Seattle, WA, USA. ✉e-mail: ks.burch@bc.edu

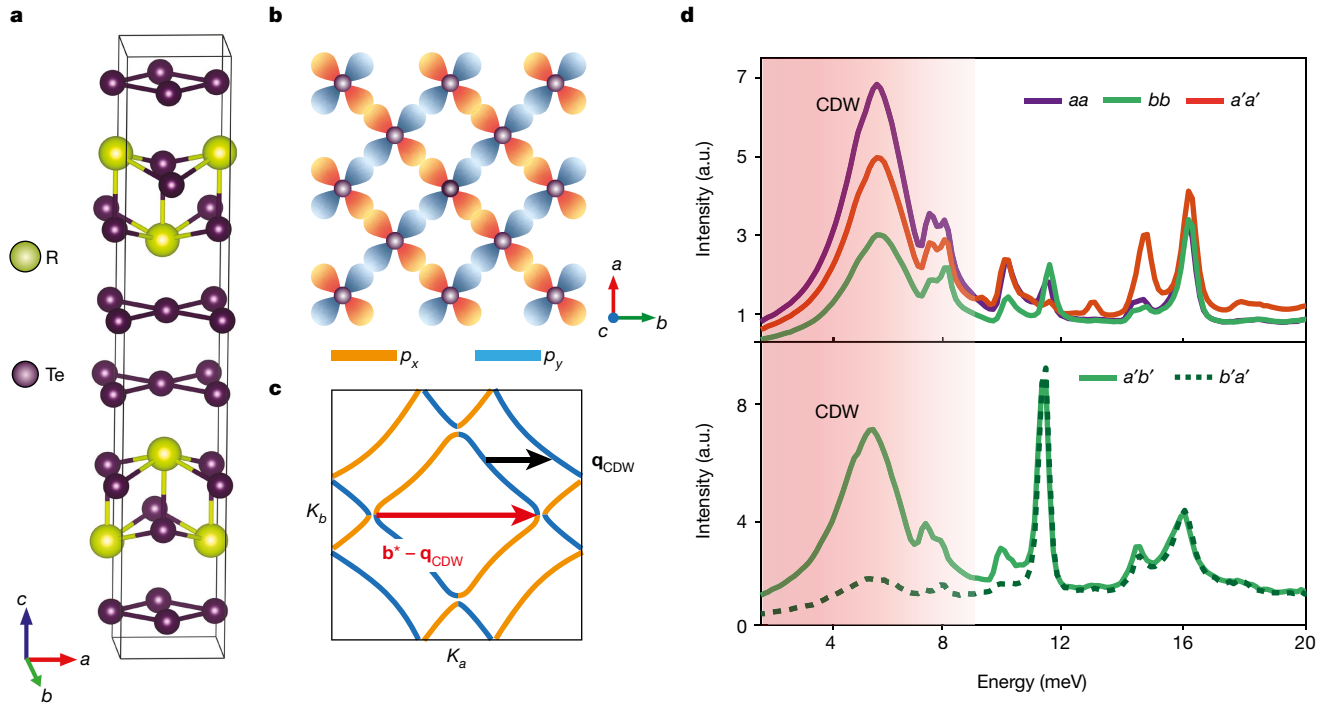

Fig. 1 | RTe_3 structure and representative Raman spectra. a, RTe_3 crystal structure and unit cell (black line). **b**, p_x (orange) and p_y (blue) orbitals in the Te layer. **c**, Fermi surface versus in-plane momentum (K_a, K_b) with orbital content labelled using the same colours as in **b**. The black arrow indicates the CDW vector ($\mathbf{q}_{CDW}$) with the red arrow indicating the second nesting condition with the reciprocal lattice vector ($\mathbf{b}^* - \mathbf{q}_{CDW}$). **d**, Raman spectra at 300 K of $GdTe_3$. Top plot is taken in parallel-linear polarization, with incident and scattered light aligned with different crystal axes. The Higgs mode and CDW folded phonons are shaded. The bottom plot is taken in cross-linear polarization, for incident light aligned with the a' (45° off a axis) direction and scattered light along b' (45° off b axis) direction (green solid line). On swapping the incident and scattered polarization (dashed line), the response of all phonons modes is identical, whereas the amplitude mode is suppressed.

Rare-earth tritellurides

We focused on the CDW system RTe_3 (R = Gd, La), exploiting its high transition temperatures ($T_{CDW}^{Gd} = 380$ K, $T_{CDW}^{La} > 600$ K), unidirectional CDW and multiple nesting conditions, which enable quantum pathway selection. The RTe_3 crystal structure consists of double layers of van der Waals-bonded square-planar Te sheets separated by RTe slabs (Fig. 1a), with an orthorhombic structure in the space group *Bmmb*. RTe_3 is nearly tetragonal ($a - b \approx 0.01$ Å)[6] with an incommensurate CDW propagating along the b axis (confirmed via transmission electron microscopy (TEM); Supplementary Information). The bands near the Fermi energy are mainly composed of the p_x and p_y orbitals of the tellurium sheet (Fig. 1b), as the p_z orbital is much lower in energy. Because the RTe_3 slab is less densely packed within the ab plane, the chosen unit cell (Fig. 1a) results in the Fermi surface shown in Fig. 1c, in which hybridization between the two orbitals happens only at isolated points due to next-nearest-neighbour interaction[36].

The incommensurate CDW ordering vector ($\mathbf{q}_{CDW}$) is (2/7)$\mathbf{b}^*$, where $\mathbf{b}^*$ is the reciprocal lattice vector, consistent with nesting between the original p_x-derived band of the Te sheet and the folded p_x band of the three-dimensional, enlarged unit cell[4,5]. Another nesting condition arises from the reciprocal lattice vector, where $\mathbf{b}^* - \mathbf{q}_{CDW}$ connects $p_x(p_y)$- to $p_y(p_x)$-derived bands. Due to the orthorhombicity, these nesting conditions are not satisfied along the a axis. Thus the CDW gap has a node, suggesting an unconventional order. Similarly, the requirement to change angular momentum when connecting the p_x to p_y states with $\mathbf{b}^* - \mathbf{q}_{CDW}$ implies that the Higgs mode has finite angular momenta. The interference between the two pathways associated with this mode, the axial nature of the Higgs, the sign change of the gap (that is p-wave order) and the unconventional CDW have yet to be explored.

As seen in Fig. 2a, b, the intermediate states have either the same or different angular momenta and thus follow different selection rules. The selection rules depend on the polarization relative to the crystal axis, the presence of single domains and clean surfaces. We achieved this with our low-temperature glovebox Raman system (Methods)[37,38], which ensured that the sample surface was free from contamination and enabled identification of the crystal axes using the sharp edges (see Supplementary Information).

Raman results

Turning to the polarization dependence of the Higgs mode, Fig. 1d shows representative Raman spectra using a 532 nm excitation of $GdTe_3$ at 300 K in parallel and cross-polarization configurations. For example, ab (xy 0°) refers to the incident (scattered) light polarized along the crystal $a(b)$ axis. Similarly, $a'b'$(xy 45°) represents the crystal rotated by 45 degrees from the ab configuration, where $a' = a + b$, $b' = a - b$. The 5 meV broad peak is the CDW Higgs mode and all other sharp peaks are phonons. The shaded region indicates the Higgs and CDW folded phonons. Both the phonons and the Higgs mode are observed in parallel polarization along aa (xx 0°), bb (xx 90°) or $a'a'$ (xx 45°) directions. Typically, the phonon modes have the same intensity when the configuration is changed from $a'b'$ (xy 45°) to $b'a'$(xy 135°). Indeed, the measured Raman intensities (I) for a given excitation are proportional to the square of the product of incident light polarization ($\hat{e}_i$), Raman tensor (R) and the scattered electric field ($\hat{e}_f$): $I = |\hat{e}_i \cdot R \cdot \hat{e}_f|^2$.

However, the Higgs mode behaves quite differently. As seen in Fig. 1d, the scattering intensity of the Higgs is strong in $a'b'$ but dramatically reduced in $b'a'$. Other than the CDW Higgs mode, phonons coupling with the CDW at 7.4 meV and 10.7 meV also showed intensity difference between $a'b'$ and $b'a'$ configurations. The Higgs mode is strongly

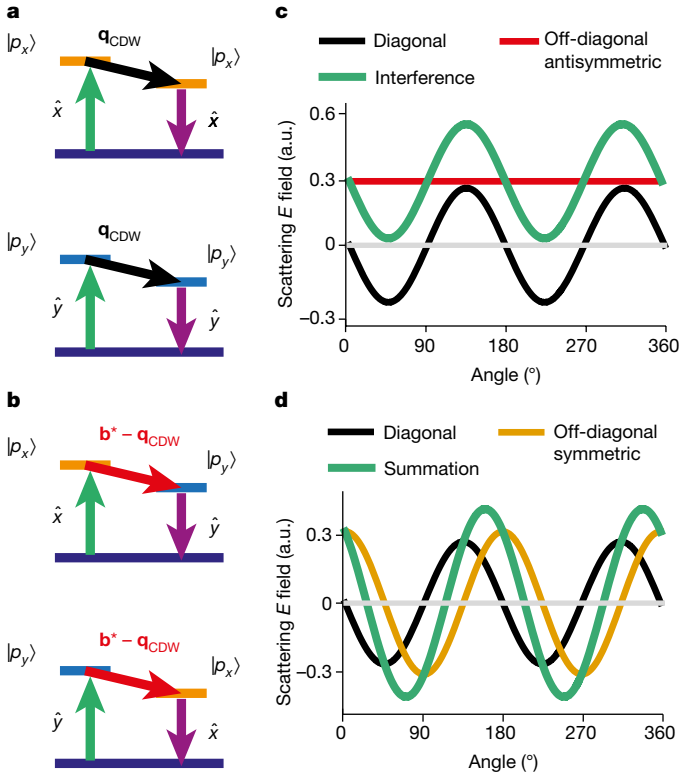

Fig. 2 | Interference of quantum pathways. a, CDW-involved symmetric Raman scattering process. **b**, CDW-involved antisymmetric Raman scattering process. **c**, Scattered electric (E) field resulting from quantum interference of a diagonal (R_{ii}) and antisymmetric off-diagonal ($R_{ij} = -R_{ji}$) Raman processes. **d**, Scattered electric (E) field resulting from quantum interference of a diagonal (R_{ii}) and symmetric off-diagonal ($R_{ij} = R_{ji}$) Raman processes. The presented angle is the polarization rotation angle relative to the crystal a axis.

mixed with 7.4 meV and 10.7 meV phonons[39], and they disappear above the CDW transition temperature[36]. Four other modes (7.9, 9.3, 9.9 and 15.9 meV) revealed responses in xx, which also appear anomalous. However, the 9.3 meV mode strongly overlaps with the Higgs, and as such it is hard to accurately extract its full angular dependence. For the other three modes, we find that their angular dependence is straightforwardly described by nearly or accidentally degenerate A_g and B_g phonons. Nonetheless, the angular dependence in xy polarization of the four phonons behaves as expected for B_g modes (four-fold symmetry). Thus their response does not affect our main conclusions (see Supplementary Information).

To understand the change in the Higgs mode intensity on swapping the incident and scattered polarization, it is useful to consider the role of the CDW in the RTe_3 quantum pathways. From symmetry, the inelastic, $q \approx 0$ excitations must fall in one of the irreducible representations $\Gamma_{Raman} = A_g + B_{1g} + B_{2g} + B_{3g}$ leading to a symmetric Raman tensor ($R_{ij} = R_{ji}$)[40]. As seen in Figs. 2 and 3, this produces a four-fold angular dependence of the intensity of the phonon modes in xy. However, due to the periodicity of the CDW, there are two quantum pathways that involve different intermediate states separated by $|\mathbf{q}_{CDW}|$ or $|\mathbf{b}^* - \mathbf{q}_{CDW}|$ (Figs. 1c and 2a, b). First, an $x(y)$ polarized incident photon excites the electron into an intermediate state $|p_x\rangle(|p_y\rangle)$, which is scattered to a $|p_x\rangle$ ($|p_y\rangle$) state by the Higgs mode with wave vector $\mathbf{q}_{CDW}$. Subsequently, the electron recombines with a hole and emits an $x(y)$ polarized photon. Such a process results in a symmetric response, as it involves scattering between states with identical polarization. Although the symmetric response could be a Raman tensor with the form of A_g, B_g or a sum of the two, in fitting the Higgs mode angular dependence, we find that the off-diagonal symmetric terms (B_g vertex) are nearly zero.

The second scattering pathway involves a Higgs mode connecting $|p_x\rangle$ ($|p_y\rangle$) to states with different angular momenta $|p_y\rangle$($|p_x\rangle$) via $|\mathbf{b}^* - \mathbf{q}_{CDW}|$. The change in angular momenta suggests that the Higgs mode requires an axial vector representation. Nonetheless, on recombination, a $y(x)$-polarized photon is produced. Noting that the excitation from the $|p_z\rangle$ band to $|p_x\rangle$ or $|p_y\rangle$ bands matches the visible excitation laser energy[5], the Higgs mode is a resonant electronic response. This resonance, combined with the angular momentum change, induces a non-zero antisymmetric (namely, $R_{ij} = -R_{ji}$) contribution to the Raman tensor[30], which by itself would produce a signal only in xy and not in xx configurations. Ultimately the interference of this antisymmetric process with the symmetric diagonal component produces the two-fold response in the cross-polarized Raman. In the Supplementary Information our calculation reproduces the asymmetric transition, depending on the pathway. This asymmetry primarily comes from the points in the Fermi surface with nesting vector $\mathbf{b}^* - \mathbf{q}_{CDW}$ and is enhanced by the orbital mixing due to next-nearest-neighbour interaction[36]. Fitting the experimental data we found a Raman tensor for the Higgs mode:

$$R_{CDW} = \begin{pmatrix} 0 & d & 0 \\ -d & 0 & 0 \\ 0 & 0 & 0 \end{pmatrix} + \begin{pmatrix} e & 0 & 0 \\ 0 & f & 0 \\ 0 & 0 & g \end{pmatrix} = \begin{pmatrix} e & d & 0 \\ -d & f & 0 \\ 0 & 0 & g \end{pmatrix},$$

where d, e, f and g are independent coefficients. Here we briefly describe the key results (details are in the Supplementary Information). The $|p_x\rangle \rightarrow |p_x\rangle$ pathway gives the same response for $a'b'$ and $b'a'$ configurations: $I = |(e-f)|^2$. However, $|p_x\rangle \rightarrow |p_y\rangle$ pathway gives $I = |2d|^2$ under $a'b'$ polarization and $I = |-2d|^2$ under $b'a'$ polarization. As such, if the two pathways did not interfere (that is, intensities are added) we would not observe any difference when swapping the incident and scattered polarization (namely, four-fold Raman response in xy; Fig. 2d). However, the pathway interference produces a Higgs mode intensity $I_{b'a'} = |(e-f) + 2d)|^2$ producing the constructive interference term and $I_{b'a'} = |(e-f) - 2d)|^2$ the destructive interference term, and thus a nearly two-fold angular response in cross-polarized Raman (Fig. 2c).

Angular dependence

To reveal the quantum interference of the pathways, we focus on the Raman response angular dependence (details in Supplementary Information). The colour maps in Fig. 3a, b present parallel and cross-polarization data and the green lines are the selected polarizations. The shaded region indicates the Higgs mode. Consistent with quantum interference, these maps clearly show that the Higgs has a two-fold response. For closer examination, we plot the intensity versus crystal angle for the Higgs mode and representative phonons of A_g and B_g symmetry (Fig. 3c–e). In the Supplementary Information we derive the Raman tensor for each mode using a generic representation in the orthorhombic crystal group. We find that both the A_g and B_g phonons follow the expected angular dependence for symmetric Raman tensors with four-fold modulation.

On the other hand, the Higgs mode reveals clear two-fold, modulated intensities in both parallel and cross-polarization (Fig. 3e), which is well described by the Raman tensor R_{CDW}, where both pathways are summed. To the best of our knowledge this is the first such observation in any Raman experiment. This result highlights the utility of the full angular dependence of the Raman experiment in revealing and potentially controlling the quantum pathways in a CDW system.

Robust quantum interference

We now discuss alternative origins of the anomalous Higgs response. Two of these are the intrinsic angular momentum from the Gd moments and the competing phase with a secondary CDW in $GdTe_3$. The latter is seen for rare-earth atoms that are smaller than Gd, for which a bidirectional

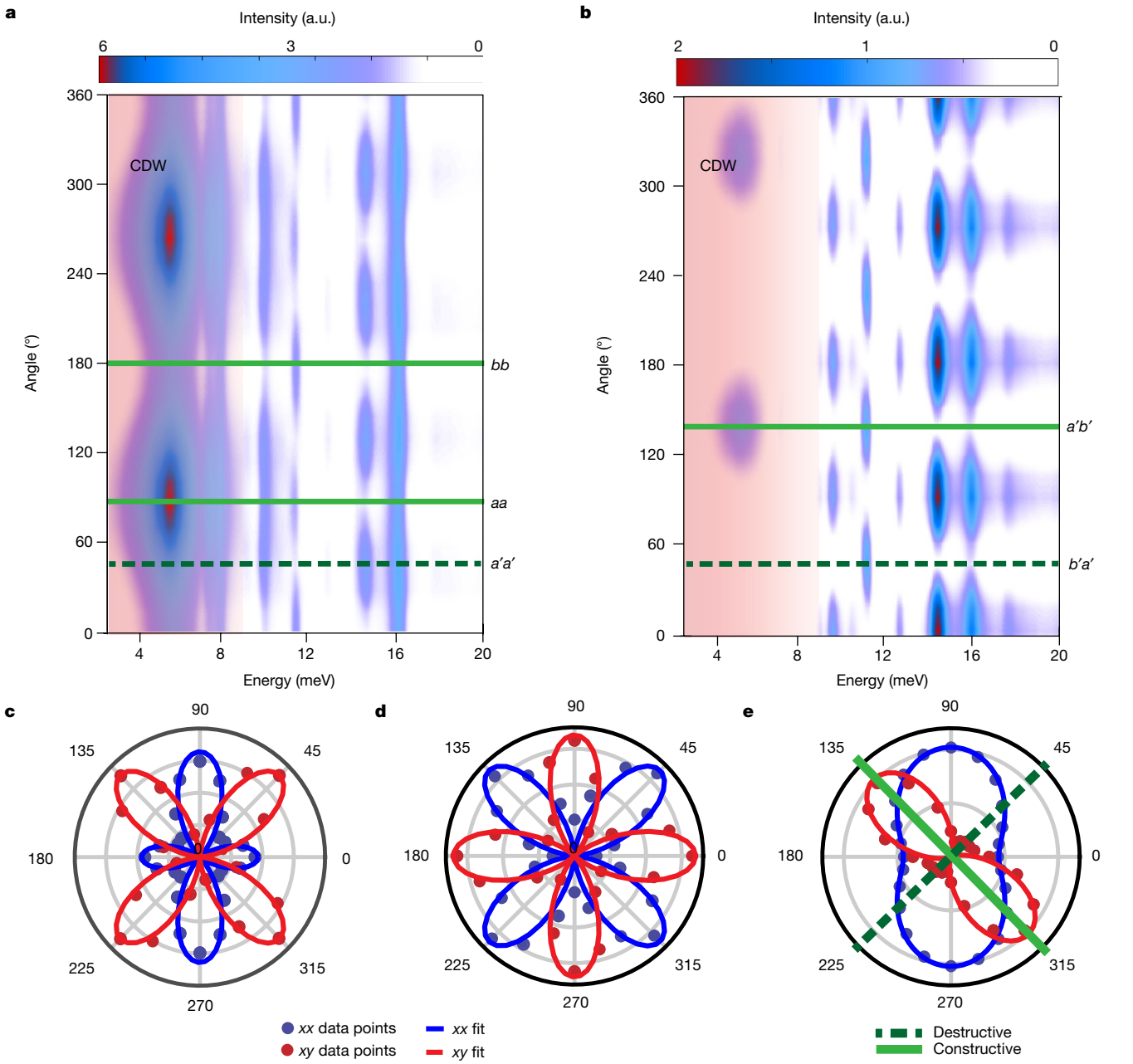

Fig. 3 | Angular-resolved Raman intensities. a, **b**, Colour map of angular-resolved Raman spectra at 300 K in parallel (**a**) and cross (**b**) linear polarization. The green lines indicate the angles of the representative spectra in Fig. 1d. **c**–**e**, Angular dependence of the ampltiudes of the Raman modes extracted from Voigt fits of the spectra in parallel (blue dots) and cross (red dots) linear polarization. **c**, A_g mode of $GdTe_3$. **d**, B_g mode of $GdTe_3$. **e**, CDW mode of $GdTe_3$ revealing the constructive (green *a′b′*) versus destructive (dashed green *b′a′*) interference.

CDW appears at low temperatures. The role of fluctuations of this bidirectional CDW is unclear. In our TEM measurements some $GdTe_3$ flakes revealed very weak secondary CDWs (see Supplementary Information).

We eliminated the complexities from Gd (magnetism and multidomains), by testing the response of $LaTe_3$, which possesses $T_{CDW} > 600$ K and contains no magnetic moments or secondary CDW. Nonetheless, as all the $LaTe_3$ have a similar electronic structure[5], the quantum pathway interference should remain. As shown in Fig. 4a, the angular dependence of the Higgs mode in $LaTe_3$ also reveals a two-fold symmetry in both parallel and cross-polarization, whereas the B_g phonon shows the expected four-fold response (Fig. 4b). The $LaTe_3$ result confirms that the interference is not due to intrinsic moments or competing phases, but from the band structure and quantum pathway selection. To ensure the reproducibility of our results, we also tested another flake, exfoliated from a different $GdTe_3$ crystal from another growth and using a separate Raman set-up with a shorter wavelength excitation laser (488 nm). As the 488 nm is still in resonance, it reveals the same angular dependence of the Raman intensity (Fig. 4c).

As a final check of the robustness of the quantum interference, we turned to the temperature dependence. Due to a large change in the Higgs mode energy, its interaction with a nearby phonon varies with temperature (Fig. 4e)[19]. Consistent with previous measurements, the Higgs intensity decreases and softens on heating. This is expected for a Higgs mode, as the free energy potential is reduced on approaching the CDW transition temperature. In addition, the Higgs mode displays an avoided crossing with the 7.4 meV phonon, which is consistent with it revealing the same symmetry as the Higgs (see Supplementary Fig. 6). This is consistent with this phonon being folded to $q = 0$ by the CDW

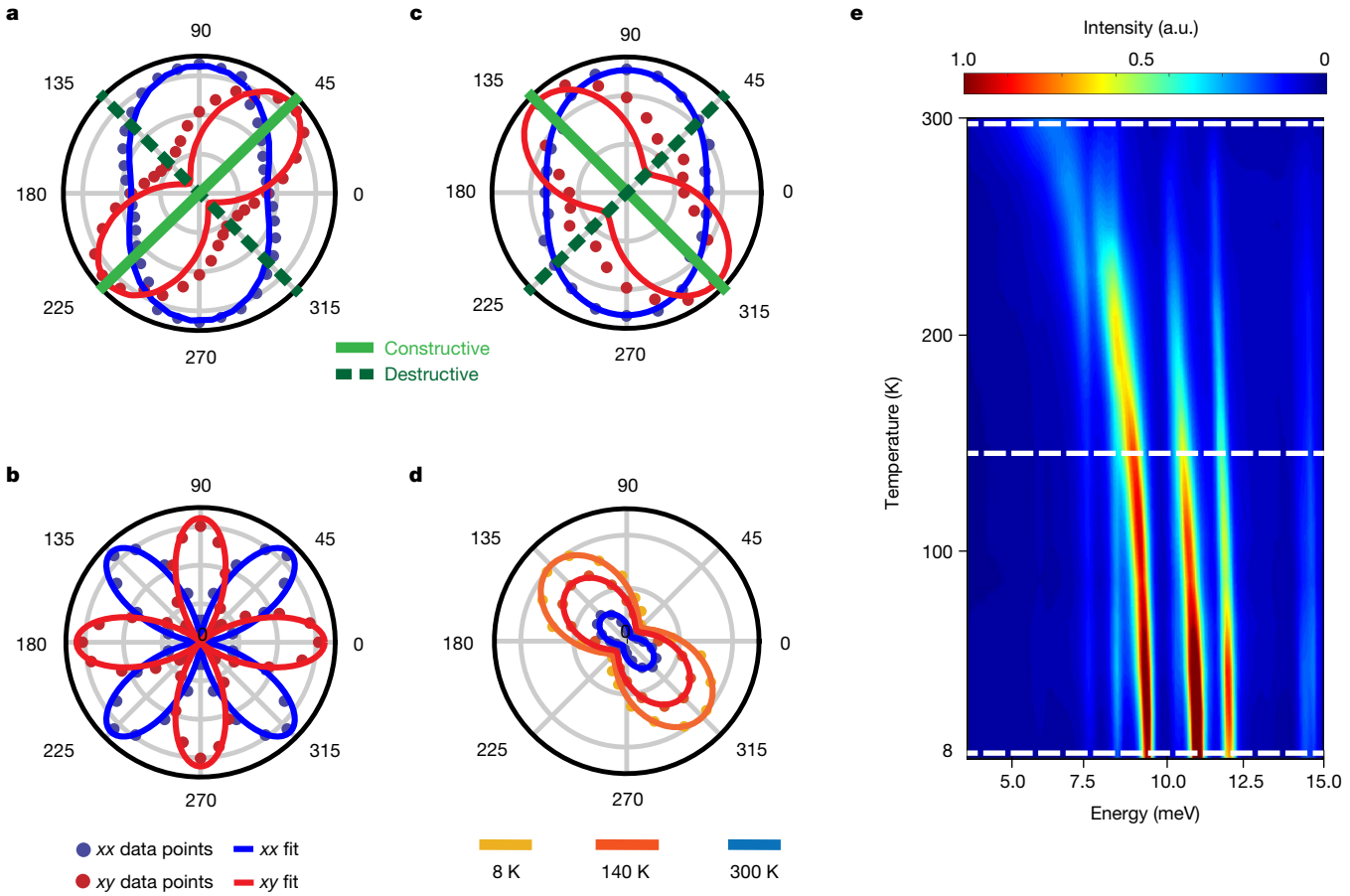

Fig. 4 | Additional tests of quantum interference in RTe_3. **a**, Angular dependence of the Higgs mode in $LaTe_3$ measured with a 532 nm excitation laser. **b**, B_g mode of $LaTe_3$ excited with a 532 nm laser following the expected angular dependence. **c**, $GdTe_3$ Higgs mode measured with a 488 nm excitation laser on a different system. **d**, The angular dependence of the Higgs intensity (dots) and fitting from Raman tensors (lines) at different temperatures, demonstrating the effect is insensitive to mixing with the neighbouring phonon mode. **e**, Temperature-dependent Raman colour map of $GdTe_3$.

and thus it undergoes the same quantum pathway interference[19,39]. Therefore, we chose three temperatures to test the quantum interference via the cross-polarization modulated intensities: 8 K, below the avoided crossing (140 K) and well above the avoided crossing (300 K). As seen in Fig. 4d, the Higgs mode has identical angular dependence at all temperatures. This demonstrates that the quantum interference is robust to the mixing of the Higgs mode with nearby phonons.

Conclusions

Our study provides the first detection of an axial Higgs mode, exploiting the quantum pathway interference in Raman scattering. The finite angular momentum of the Higgs provides compelling evidence that the charge density wave order in RTe_3 is unconventional. Using a phenomenological description of the Fermi surface, we elucidate the role of next-nearest-neighbour interaction in the observed asymmetry of Raman transitions involving a change of angular momentum. The methodology used can be applied to search for new symmetry-broken and topologically ordered states via their novel collective modes. Furthermore, the straightforward application of tuning the interference with light polarization could enable manipulation of the quantum properties of collective excitations to reveal new states.

Online content

Any methods, additional references, Nature Research reporting summaries, source data, extended data, Supplementary Information, acknowledgements, peer review information; details of author contributions and competing interests; and statements of data and code availability are available at https://doi.org/10.1038/s41586-022-04746-6.

1. Franzosi, D. B., Cacciapaglia, G., Cai, H., Deandrea, A. & Frandsen, M. Vector and axial-vector resonances in composite models of the Higgs boson. *J. High Energy Phys.* **2016**, 76 (2016).
2. Shimano, R. & Tsuji, N. Higgs mode in superconductors. *Annu. Rev. Condens. Matter Phys.* **11**, 103–124 (2020).
3. Pekker, D. & Varma, C. Amplitude/Higgs modes in condensed matter physics. *Annu. Rev. Condens. Matter Phys.* **6**, 269–297 (2015).
4. Klemenz, S. et al. The role of delocalized chemical bonding in square-net-based topological semimetals. *J. Am. Chem. Soc.* **142**, 6350–6359 (2020).
5. Brouet, V. et al. Angle-resolved photoemission study of the evolution of band structure and charge density wave properties in RTe_3 (R=Y, La, Ce, Sm, Gd, Tb, and Dy). *Phys. Rev. B* **77**, 235104 (2008).
6. Lei, S. et al. High mobility in a van der Waals layered antiferromagnetic metal. *Sci. Adv.* **6**, eaay6407 (2020).
7. Podolsky, D., Auerbach, A. & Arovas, D. P. Visibility of the amplitude (Higgs) mode in condensed matter. *Phys. Rev. B* **84**, 174522 (2011).
8. Zeilinger, A., Gähler, R., Shull, C. G., Treimer, W. & Mampe, W. Single- and double-slit diffraction of neutrons. *Rev. Mod. Phys.* **60**, 1067–1073 (1988).
9. Zhang, Y., Tan, Y.-W., Stormer, H. L. & Kim, P. Experimental observation of the quantum Hall effect and Berry's phase in graphene. *Nature* **438**, 201–204 (2005).
10. Qu, D.-X., Hor, Y. S., Xiong, J., Cava, R. J. & Ong, N. P. Quantum oscillations and Hall anomaly of surface states in the topological insulator Bi_2Te_3. *Science* **329**, 821–824 (2010).
11. Ryu, C., Samson, E. C. & Boshier, M. G. Quantum interference of currents in an atomtronic SQUID. *Nat. Commun.* **11**, 3338 (2020).
12. Cleuziou, J.-P., Wernsdorfer, W., Bouchiat, V., Ondarçuhu, T. & Monthioux, M. Carbon nanotube superconducting quantum interference device. *Nat. Nanotechnol.* **1**, 53–59 (2006).
13. Giazotto, F., Peltonen, J. T., Meschke, M. & Pekola, J. P. Superconducting quantum interference proximity transistor. *Nat. Phys.* **6**, 254–259 (2010).
14. Mittal, S., Orre, V. V., Goldschmidt, E. A. & Hafezi, M. Tunable quantum interference using a topological source of indistinguishable photon pairs. *Nat. Photonics* **15**, 542–548 (2021).
15. Wall, S. et al. Quantum interference between charge excitation paths in a solid-state Mott insulator. *Nat. Phys.* **7**, 114–118 (2011).
16. Barik, S. et al. A topological quantum optics interface. *Science* **359**, 666–668 (2018).

17. Popescu, S. Dynamical quantum non-locality. *Nat. Phys.* **6**, 151–153 (2010).
18. Chang, J. et al. Direct observation of competition between superconductivity and charge density wave order in $YBa_2Cu_3O_{6.67}$. *Nat. Phys.* **8**, 871–876 (2012).
19. Lavagnini, M. et al. Raman scattering evidence for a cascade evolution of the charge-density-wave collective amplitude mode. *Phys. Rev. B* **81**, 081101 (2010).
20. Kogar, A. et al. Light-induced charge density wave in $LaTe_3$. *Nat. Phys.* **16**, 159–163 (2020).
21. Yusupov, R. V., Mertelj, T., Chu, J.-H., Fisher, I. R. & Mihailovic, D. Single-particle and collective mode couplings associated with 1- and 2-directional electronic ordering in metallic RTe_3 (R=Ho, Dy, Tb). *Phys. Rev. Lett.* **101**, 246402 (2008).
22. Liu, H. Y. et al. Possible observation of parametrically amplified coherent phasons in $K_{0.3}M_3O_3$ using time-resolved extreme-ultraviolet angle-resolved photoemission spectroscopy. *Phys. Rev. B* **88**, 045104 (2013).
23. Zocco, D. A. et al. Pressure dependence of the charge-density-wave and superconducting states in $GdTe_3$,$TbTe_3$, and $DyTe_3$. *Phys. Rev. B* **91**, 205114 (2015).
24. Xi, X. et al. Strongly enhanced charge-density-wave order in monolayer $NbSe_2$. *Nat. Nanotechnol.* **10**, 765–769 (2015).
25. Yoshikawa, N. et al. Ultrafast switching to an insulating-like metastable state by amplitudon excitation of a charge density wave. *Nat. Phys.* **17**, 909–914 (2021).
26. Mohammadzadeh, A. et al. Room temperature depinning of the charge-density waves in quasi-two-dimensional 1T-TaS_2 devices. *Appl. Phys. Lett.* **118**, 223101 (2021).
27. Klein, M. V. Theory of Raman scattering from charge-density-wave phonons. *Phys. Rev. B* **25**, 7192–7208 (1982).
28. Wang, Y. et al. The range of non-Kitaev terms and fractional particles in α-$RuCl_3$. *npj Quantum Mater.* **5**, 14 (2020).
29. Devereaux, T. P. & Hackl, R. Inelastic light scattering from correlated electrons. *Rev. Mod. Phys.* **79**, 175–233 (2007).
30. Cardona, M. *Light Scattering in Solids 1* (Springer, 1975).
31. Koningstein, J. A. & Mortensen, O. S. Electronic Raman spectra IV: relation between the scattering tensor and the symmetry of the crystal field. *J. Opt. Soc. Am.* **58**, 1208 (1968).
32. Chen, C.-F. et al. Controlling inelastic light scattering quantum pathways in graphene. *Nature* **471**, 617–620 (2011).
33. Rivera, P. et al. Observation of long-lived interlayer excitons in monolayer $MoSe_2$-WSe_2 heterostructures. *Nat. Commun.* **6**, 6242 (2015).
34. Friedman, J. & Hochstrasser, R. M. Interference effects in resonance Raman spectroscopy. *Chem. Phys. Lett.* **32**, 414–419 (1975).
35. Chen, C., Yin, Y.-Y. & Elliott, D. S. Interference between optical transitions. *Phys. Rev. Lett.* **64**, 507–510 (1990).
36. Eiter, H.-M. et al. Alternative route to charge density wave formation in multiband systems. *Proc. Natl Acad. Sci. USA* **110**, 64–69 (2013).
37. Gray, M. J. et al. A cleanroom in a glovebox. *Rev. Sci. Instrum.* **91**, 073909 (2020).
38. Tian, Y. et al. Low vibration high numerical aperture automated variable temperature Raman microscope. *Rev. Sci. Instrum.* **87**, 043105 (2016).
39. Maschek, M. et al. Competing soft phonon modes at the charge-density-wave transitions in $DyTe_3$. *Phys. Rev. B* **98**, 094304 (2018).
40. Powell, R. C. *Symmetry, Group Theory, and the Physical Properties of Crystals* Vol. 824 (Springer, 2010).

Methods

Crystal growth

High-quality RTe_3 single crystals were grown in an excess of tellurium (Te) via a self-flux technique. Te (metal basis >99.999%, Sigma-Aldrich) was first purified to remove oxygen contamination and then mixed with the rare earth (>99.9%, Sigma-Aldrich) in a ratio of 97:3. The mixture was sealed in an evacuated quartz ampoule and heated to 900 °C over a period of 12 h and then slowly cooled down to 550 °C at a rate of 2 °C h^{-1}. The crystals were separated from the flux via centrifugation at 550 °C.

Sample preparation and vacuum transfer

$GdTe_3$ and $LaTe_3$ flakes were exfoliated and characterized using unpolarized Raman in an argon-filled glovebox. Then, they were loaded into a 10^{-6} mbar vacuum suitcase and directly transferred into a low-temperature cryostat[37]. This ensured that the sample surface was free from contamination, atomically flat, contained single CDW domains and enabled identification of the crystal axes using the sharp edges.

Angle-resolved Raman spectroscopy

The 532 nm Raman experiments were performed with a custom-built, low-temperature microscopy set-up[38]. A 532 nm excitation laser, with spot diameter of 2 μm, was used, with the power limited to 10 μW to minimize sample heating while enabling a strong enough signal. At both room and base temperature (10 K), the reported spectra were averaged from three spectra in the same environment to ensure reproducibility. The spectrometer had a 2,400 grooves per mm grating, with an Andor CCD, providing a resolution of approximately 1 cm^{-1}. Dark counts were removed by subtracting data collected with the same integration time with the laser blocked. Freshly cleaved samples were transferred to a cryostat with an optical window and pumped down to a vacuum level of 10^{-6} torr. The 488 nm (2.54 eV) emission line from an argon laser was used as the excitation source. The incident laser was reflected by a 90/10 non-polarizing cube beam splitter and then focused to a spot size of 2 μm on the sample using a ×50 objective lens (numerical aperture, 0.35). The laser power on the sample was 700 μW. The incident beam and collected optical signal were linear polarization resolved using a combination of Fresnel rhomb retarders and linear polarizers. The Raman signal was dispersed by a Horiba T64000 spectrometer equipped with a gratings with 1,800 grooves per mm, and detected with a liquid-nitrogen-cooled CCD camera. We used a Fresnel rhomb to measure the angular-dependent Raman spectra in both set-ups.

Data availability

The datasets generated and/or analysed during the current study are available from the OSF storage https://osf.io/87bxy/.

Acknowledgements We thank L. Benfatto and A. Chubukov for useful discussions about the CDW Raman response. Y.W. is grateful for the support of the Office of Naval Research under award number N00014-20-1-2308. K.S.B. and L.M.S. acknowledge joint support by the Air Force office of Scientific Research under award number FA9550-20-1-0246. The work of G.M. was supported by the National Science Foundation via award DMR-2003343. M.M.H. acknowledges the primary support of the US Department of Energy (DOE), Office of Science, Office of Basic Energy Sciences under award number DE-SC0018675. L.M.S. acknowledges support from the Gordon and Betty Moore Foundation (EPiQS Synthesis Award) through grant GBMF9064, the David and Lucile Packard Foundation and the Sloan Foundation. J.J.C. and J.L.H. gratefully acknowledge support from the Gordon and Betty Moore Foundation (EPiQS Synthesis Award). Y.-C.W. and J.Y. are supported by the National Science Foundation under award number DMR-2004474. Work by D.X. is supported by DOE award number DE-SC0012509. I.P. and P.N. are primarily supported by the Quantum Science Center (QSC), a National Quantum Information Science Research Center of the US DOE. Theory by I.P. and P.N. is supported by the QSC. I.P. was partially supported by the Swiss National Science Foundation (SNSF) under project ID P2EZP2_199848. P.N. is a Moore Inventor Fellow and gratefully acknowledges partial support through grant GBMF8048 from the Gordon and Betty Moore Foundation.

Author contributions Y.W. performed the Raman experiments and analysed the data. G.M. helped with data fitting and plotting. S.L. and L.M.S. grew the crystals. Y.-C.W. and J.Y. helped with 488 nm Raman measurement. J.L.H. and J.J.C. performed TEM measurements. I.P. and P.N. developed the theory with input from H.L. and D.X. Y.W. and M.M.H. wrote the manuscript with the help of K.S.B. K.S.B. conceived and supervised the project.

Competing interests The authors declare no competing interests.

Additional information
Supplementary information The online version contains supplementary material available at https://doi.org/10.1038/s41586-022-04746-6.
Correspondence and requests for materials should be addressed to Kenneth S. Burch.
Peer review information *Nature* thanks Marie Aude Measson, Tommaso Cea and the other, anonymous, reviewer(s) for their contribution to the peer review of this work. Peer reviewer reports are available.